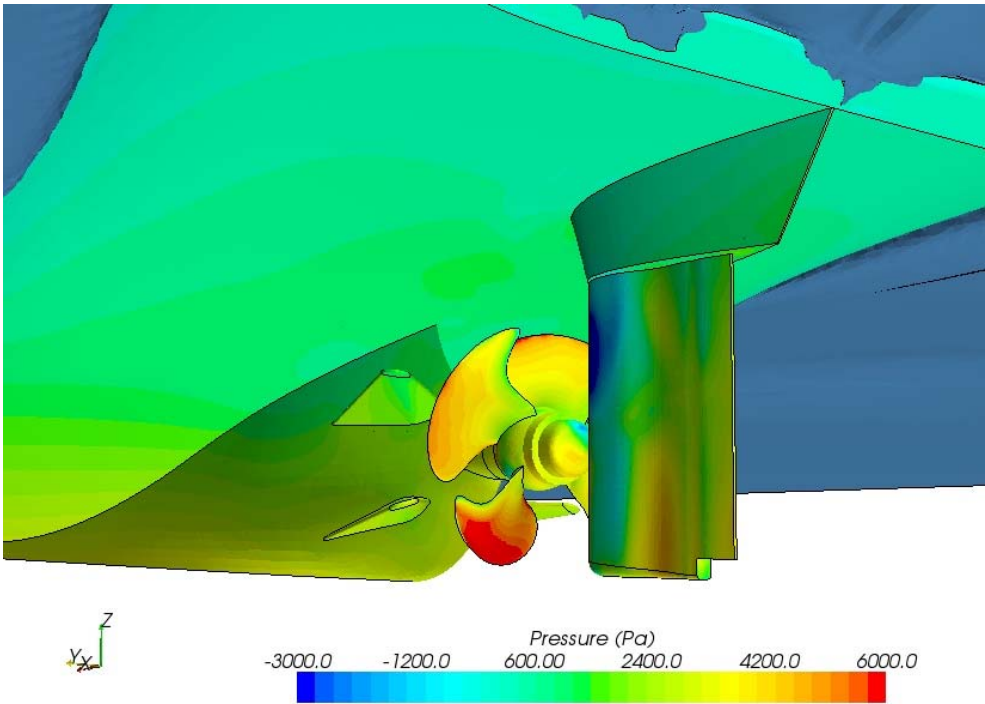


Final Report

CFD Project

FORCE 187DCMT



Project No. and Title of Report:

DCMT

**NUMERICAL FLOW SIMULATION OF MODEL SHIP WITH APPENDAGES.
METHOD, VALIDATION AND INVESTIGATION OF THE FLOW AROUND HULL,
RUDDER AND PROPELLER**

Client:
DCMT

Client's Ref.:

Author(s):
Claus Daniel Simonsen
Rasmus Carstens

Date: 2009-01-07

Approved by:

<i>Revision</i>	<i>Description</i>	<i>By</i>	<i>Checked</i>	<i>Approved</i>	<i>Date</i>
A	Final version	CDS			

Keywords:
CFD Calculations
Rudder, Propeller and Hull

Classification:
 Open
 Internal
 Confidential



TABLE OF CONTENTS

PAGE

1. INTRODUCTION 1

2. APPROACH AND METHODS 2

2.1 PLANNING AND DEFINITION OF OVERALL PROCEDURE..... 3

2.2 MODELING OF THE PROPELLER-ALONE CONDITION..... 3

2.3 MODELING OF THE HULL-ALONE CONFIGURATION 3

2.4 ASSEMBLY AND SETUP OF COMBINED HULL AND PROPELLER MODEL WITH AND WITHOUT FREE SURFACE..... 4

2.5 INCLUSION OF CAVITATION MODEL IN PROPELLER/HULL MODEL..... 5

2.6 NUMERICAL METHOD..... 5

2.7 BENCHMARK SHIP AND COMPUTATIONAL GRIDS 5

3. OPEN-WATER SIMULATION..... 7

4. BARE HULL SIMULATION – WITH AND WITHOUT ICE FINS..... 8

5. APPENDED HULL SIMULATION – CAVITATION TUNNEL SETUP 9

6. APPENDED HULL SIMULATION – TOWING TANK SETUP..... 12

7. CAVITATION SETUP..... 17

8. SUMMARY AND CONCLUSIONS..... 18

9. LITERATURE 19

1. Introduction

Together with MEK, DTU, FORCE Technology has formed "Dansk Center for Maritim Teknologi" [Danish Centre for Maritime Technology] (DCMT), which is funded by the Danish Maritime Foundation and which runs over a five years period. The objective of the centre is to promote Danish know-how within maritime technology through increased research and development in the maritime industry. Further, it is DCMT's purpose to raise interest in the maritime engineering degrees to ensure an inflow of competent and innovative engineers to the "Blue Denmark".

Since 2000 FORCE Technology has had great success with application of non-linear potential flow calculations for optimisation of hull lines, and is today a

world leader within this field. In parallel FORCE has co-operated closely with IIHR (Iowa Institute of hydraulic research) in USA for almost 10 years. The work, sponsored by ONR (Office of Naval Research), has been focused on development and application of RANS-based CFD codes for solution of flow problems around a ship hull, especially regarding manoeuvring. Due to these activities FORCE has gained considerable experience within application of RANS based CFD based for calculations of flows around a ship hulls.

MAN-Diesel (Frederikshavn) has valuable experience in design and production of complete propulsion systems including propeller. For many years MAN-Diesel has been using traditional 'lifting-line' theory for propeller design, but recently MAN-Diesel has started using RANS-CFD for

optimisation of propeller and nozzle designs.

Because of the constant development of commercial RANS-CFD tools and related grid generation tools FORCE sees a potential in applying RANS-CFD for solution or optimisation of flow problems around ship hulls and propellers. Therefore, FORCE wanted to start a project aiming at validation of RANS-CFD codes in connection with design of ships and/or propellers. In this project it is investigated and demonstrated how RANS can be used for calculation of the flow around a hull with rotating propeller. Further, comparisons with model test data give an indication of how well the simulation agrees with the measured data.

2. Approach and methods

Modeling the propulsion system of a ship is a complicated task. Partly due to large numerical models involved and partly due to limited experience within this type of application. Therefore, it has been necessary to build the model step by step and gradually increase complexity throughout the project. This procedure allows for thorough testing of the method, and simultaneously enhances knowledge and experience.

Before the computational approach is used with alternative geometries it must be built and tested on a representative test ship with available experimental results from open water, resistance, self-propulsion and cavitation experiments.

For the sake of validation of the results obtained in this project, a benchmark ship is therefore chosen. The benchmark ship is described in more detail later in this report.

The below-mentioned activities describe the applied stepwise procedure that was used to build up the final numerical model in order to demonstrate the capabilities of RANS in connection with

simulation of rudder-propeller-hull configurations:

1. A CFD model of the propeller geometry is build and tested in an open-water setup in order to be compared with data from an experimental open water test carried out in the model basin at FORCE technology.
2. A CFD model of the hull and rudder geometries is build and tested in a resistance test setup in order to be compared with data from a resistance test carried out in the model basin at FORCE technology.
3. Based on the results and experience gained in 1 and 2 the two models are combined into one model containing both the propeller and the hull. The data exchange between the rotating propeller geometry and the static hull model is obtained by means of the sliding interface approach.
4. The combined model from step 3 is initially tested in a "cavitation tunnel" setup. This allows the problem to be simplified by omitting the effect of the free surface and keep focus on the coupling. The computations are performed at atmospheric pressure, which means that cavitation does not occur. The results from this calculation cover primarily propeller thrust and torque and the computed results are compared with model test data from a similar test conducted at SSPA in Sweden.
5. In this step the combined model is finally tested in a "resistance and self-propulsion" setup, which is more complicated than step 4, since the effect of the free surface is included. The results from this calculation cover primarily resistance plus propeller thrust and torque and the computed results are compared with model test data from a similar test conducted in FORCE Technology's towing tank.
6. The final task in the project covers cavitation simulation. The aim of this activity is to see if a RANS model is

capable of capturing the cavitation on the propeller blades and in the down stream tip vortices. It should be noted that investigation of cavitation was not the primary goal of the project, so the work done in this task is limited.

Common for all computations is that they are done in model scale as is common practice with RANS-based CFD. There is no solid experience base for full-scale calculations for ships, as these demand very large numerical models to be able to resolve the flow in the near wall boundary layer. However, the few examples in literature indicate that the actual calculation can be run at relatively coarse grids, but as there are no full-scale data available for validation of the methods, it is difficult to estimate the quality of such simulations.

The individual activities in step 1 through 6 are described in more detail below.

2.1 Planning and definition of overall procedure

MAN Diesel and FORCE Technology have access to the same RANS software packages (Star-CCM+) for calculation of flow problems. The use of the same software packages facilitates the coupling between the hull and propeller model, as numerical grid formats will be the same. Yet it was necessary to decide on for instance final data exchange formats, turbulence models, grid types and grid density, discretization schemes and geometric limitations related to mesh generation to determine the coupling procedure. Mapping of requirements to the ship and propeller models were therefore made in the first phase of the project so that hull and propeller model could be built up individually, but with later coupling in mind. Further it was decided, for the ship in question, which conditions should be calculated.

2.2 Modeling of the propeller-alone condition

Based on conditions and interface approach laid out in step 1, MAN Diesel generated the computational grid for the propeller alone. This also included the necessary grids for study of grid fineness influence on the calculated flow. These grids were then used to make open-water calculations for the propeller. For convenience the applied computational meshes were designed so they, with a minimum of modifications, could be used for production runs when the complete propeller/hull model was built and tested later.

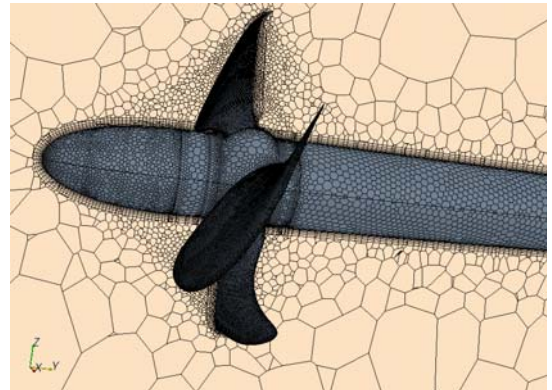


Figure 1: *Illustration of grid used for open water calculation.*

In order to validate the calculated results and get an idea about how the numerical tools performed, the results were compared with experimental data. This means that propeller thrust and torque were compared to measured open-water data as described later in the report.

2.3 Modeling of the hull-alone configuration

In step 2 FORCE built up a grid around the hull with appendages, i.e. rudder and fins. Again the grids were designed to be applicable to studies of grid dependence. Also here the aim was to design the computational grids so they, with a minimum of modifications, could

be used for production runs with the later complete total propeller/hull model. It should be noted that the ship was fixed during the calculation, i.e. dynamic sinkage and trim were not solved for. However, in order to account for sinkage and trim the ship was positioned according to the measured values, which means that the computational mesh was generated around the ship in the position it would be in, when sailing.

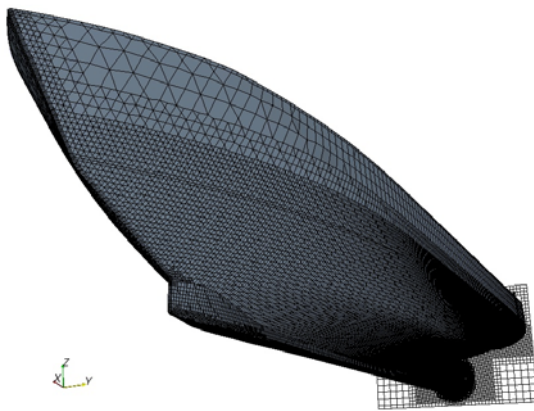


Figure 2: *Illustration of the grid used for the hull calculation.*

2.4 Assembly and setup of combined hull and propeller model with and without free surface

Based on the learning from steps 1 and 2 the propeller was joined with the hull in order to simulate the cavitation tunnel setup at atmospheric pressure and the self-propulsion setup.

In order to join the two components, the idea was to make a cylindrical hole in the hull grid at the propeller position. In this hole a cylindrical grid domain containing the propeller, hub and shaft was inserted. For this type of model it is not a requirement that the points in the propeller and hull grids meet point to point on the boundary between the two domains; thus the two grids can be built independently. Yet they must have boundary cells of comparable size in

order to secure a stable exchange of boundary data between the hull and propeller grids.

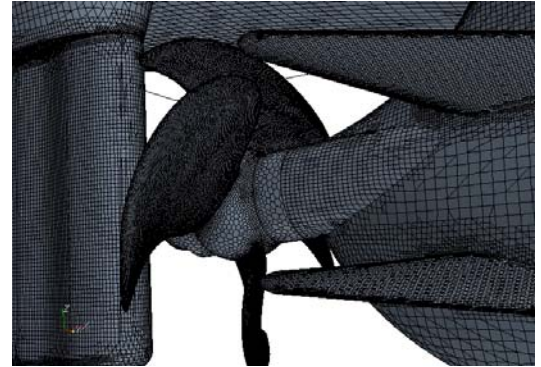


Figure 3: *Illustration of surface grid on the combined hull-propeller-model.*

In order to simulate the rotating propeller the 'rigid body motion' approach was used. This means that the whole propeller domain rotates with a speed equivalent to the propeller's speed of rotation. To allow exchange of data on the boundaries between the hull and propeller domains, it was necessary to use "sliding meshes", which means that the connectivity is calculated and updated in each time step.

The above procedure required that the computation was run in transient mode. In this connection it should be noted that small time steps are required to model the propeller which is rotating with relatively high speed. The time step in the present simulations was set in order to obtain a propeller rotation of 2 to 4 degrees per time step. In terms of time step this corresponds to steps in the order of 10^{-4} second. However, this time step size is critical from the point of view of the overall computational time. The reason is that in order for the "global" flow around the hull to build up, it is not unusual that the flow must be calculated for a period of time equivalent to the time it takes for the ship to sail 2 to 3 ship lengths. If this start-up time has to be simulated with time steps determined by the propeller, many hours of calculations will be required. To overcome this issue it was attempted to simulate the start-up time for the ship with larger time steps while the propeller

was brought to a standstill or only rotated slowly. Then after the boundary layer on the hull was built up, the time step was reduced and the propeller was given the correct rotational speed.

Concerning the free surface, two different approaches were used. One was to omit the free surface to limit the complexity and the size of the numerical model. In this case only the under-water part of the hull is considered and the free-surface boundary condition is replaced by a symmetry condition on the still water surface. This approach allows comparison with measured propeller data from the cavitation tunnel, but not with resistance. Another approach was to include the free surface and the part of the hull above the water. By doing this it was both possible to compare measured propeller quantities and resistance.

The propeller RPM used in the simulations were set at the values used during the model tests. Therefore, it was not necessary to search for the self-propulsion point. This saves resources, since a calculation of the self-propulsion point will require an iterative procedure where the propeller revolutions are adjusted so that the propeller thrust balances the resistance. With the expected long calculation times this approach was considered too time-consuming.

2.5 Inclusion of cavitation model in propeller/hull model

The work under activity 6 listed above was done in order to setup a numerical cavitation model based on RANS. The purpose of this simulation was to investigate if the present RANS-model is capable of solving the flow when cavitation occurs. The results from the cavitations simulations were compared qualitatively with results from a cavitation test carried out at SSPA in Sweden.

Neither MAN Diesel nor FORCE has strong experience in use of the cavitation model in the CFD software and the cavitation simulation was not in the scope of the project. However, it was decided to turn on the cavitation model to perform an initial study of this type of simulation.

2.6 Numerical method

The computations were performed with the Reynolds Averaged Navier-Stokes (RANS) solver StarCCM+ from CD-adapco. The code solves the RANS and continuity equations on integral form on a polyhedral mesh by means of the finite volume technique. Both steady state and transient calculations are considered. For the steady state calculations the temporal discretization is based on a first order Euler difference, while a second order difference is used for transient calculations. Spatial discretization is performed with second order schemes for both convective and viscous terms. The pressure and the velocities are coupled by means of the SIMPLE method. Closure of the Reynolds stress problem is achieved by means of the iso-tropic blended $k-\epsilon/k-\omega$ SST turbulence model with an all Y^+ wall treatment. The rotating propeller was treated in different ways. For open-water calculations the propeller inflow was uniform, so the moving reference approach was applied, i.e. the blade velocity was set on the propeller blades and centripetal effects are included in additional source terms in the momentum equations. For the propeller rotating behind ship, a rigid body approach was applied. The free surface was modeled with the two phase volume of fluid technique (VOF). For the cavitation modeling, it is based on the Rayleigh-Plasset model. Further details about the code can be found in [3].

2.7 Benchmark ship and computational grids

The study is carried out for a model of a 70m inspection vessel with appendages and propeller.

The model is in scale 1:14.15. The main particulars and propeller data are shown in Table 1 Ship speed and propeller RPM are given in the relevant sections describing the different simulations.

L_{pp} (m)	4.3107
B (m)	1.0325
T (m)	0.3495
S (m^2)	5.4895
C_b	0.44
D_p (m)	0.2332
Z (no.of blades)	4
$P_{0.7}$	1.2018

Table 1. Hull and propeller data.



Figure 4. 70m inspection vessel.

Figure 4 shows a picture of the inspection vessel on sea trail.



Figure 5. Model rudder-propeller arrangement.

Figure 5 shows a picture of the ship model build at FORCE Technology in

Lyngby. The numerical model similar to this picture can be seen in Figure 7.

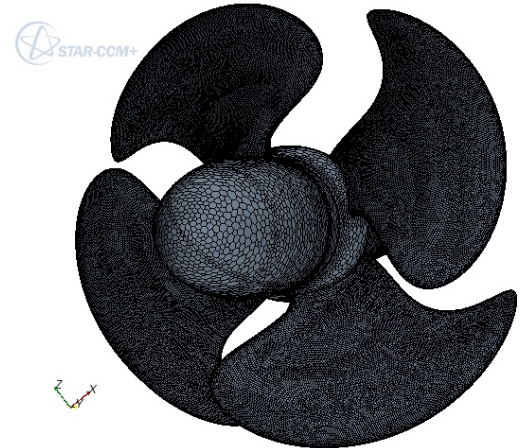


Figure 6. Computational grid on propeller.



Figure 7. Computational grid on hull and propeller.

Concerning the grid, the computations are performed with unstructured grids generated in Star-CCM+. The propeller is modeled with a polyhedral mesh, Figure 6. The open-water mesh consists of approximately 2 million cells. The ship is modeled with a trimmed mesh, which is a hexa-dominant polyhedral mesh. The mesh for the ship alone contains approximately 3.4 million cells. Since the propeller is running behind the ship, both sides are considered instead of exploiting the centre plane symmetry. The grid for the complete hull-propeller model is shown in Figure 7. The near wall spacing of the grids on no-slip

surfaces are in the range from $y^+ \approx 1$ to $y^+ \approx 30$. Concerning verification, a grid refinement study was made for the hull alone and the propeller alone. Error estimates with unstructured grids are not possible, since systematic refinement cannot be performed. However, by changing the reference length used in the mesh generation tool, a semi-systematic refinement was done in order to check the trend of the solution changes with the fineness of the mesh.

3. Open-water simulation

The open water test is carried out at the same running conditions as used in the experimental set up at FORCE Technology. The solution domain is chosen to extend 10 propeller diameters in front of the propeller, 18 diameters in the radial direction and 30 diameters behind the propeller. The flow solver is run in steady mode and the rotation of the propeller is accounted for by using the moving reference frame approach. This approach works fine in open water, where the propeller sees a completely uniform inflow field. The calculation is carried out for advance coefficients in the range from $J=0.0$ to $J=1.1$.

Like the experiment the computed thrust and torque on the propeller are converted into the dimensionless thrust coefficient K_t , torque coefficient K_q and the open water coefficient η_0 is calculated. The advance ratio J and the three coefficients are defined as

$$J = \frac{U_a}{nD} \quad (1)$$

where U_a is the speed of advance, n is the propeller revolution rate and D is the propeller diameter.

$$K_t = \frac{T}{\rho n^2 D^4} \quad (2)$$

where T is the measured thrust and ρ is the water density.

$$K_q = \frac{Q}{\rho n^2 D^5} \quad (3)$$

Q is the measured torque.

$$\eta_0 = \frac{J K_t}{2\pi K_q} \quad (4)$$

With respect to the grid study, it shows that the calculated K_t changes with 2.7% when going from coarse to medium grid, while the change is reduced to 1.3% when going from medium to fine grid. For K_q the changes are 3.2% and 1.6% from coarse to medium and medium to fine, respectively. The number of cells in the fine mesh, which was used for the final open water calculation, is 1,963,001.

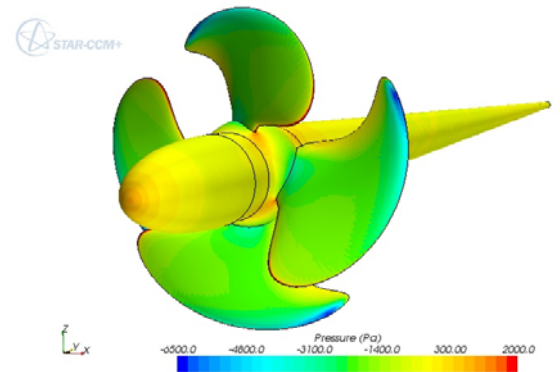


Figure 8. Pressure distribution on suction side of propeller.

For the results of the open water calculation, a study of the flow field shows that the propeller, as expected, accelerates the flow over the blades and introduces swirl in the flow downstream of the propeller. On the blades themselves the pressure field shows low pressure on the suction side and high pressure on the pressure side. Figure 8 illustrates the pressure distribution on the suction side of the open water propeller.

Figure 9 shows the calculated open water curves together with the measured curves from [4].

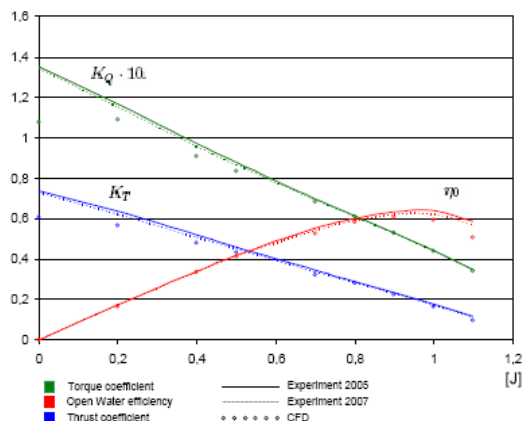


Figure 9. Computed and measured open-water curves.

Two sets of measured data are shown. The first set was measured in 2005, but the test was repeated in connection with the present project to check the repeatability of the measurement and as seen the two data sets are in fairly good agreement. When it comes to a comparison between the calculated and measured data, it is seen that fairly good agreement is achieved. Particularly in the region around $J=0.8$, which is the point where the ship usually operates.

J	Kt	Kq x 10
0.0	17.853	20.484
0.2	10.935	6.538
0.4	7.479	6.607
0.5	6.066	4.716
0.7	6.531	2.267
0.8	3.412	0.516
0.9	4.568	-0.208
1.0	7.898	0.896
1.1	15.439	1.987

Table 2. Difference between CFD and measurement in %.

Table 2 summarizes deviations between the two data sets. It is seen that the deviations increase as J is reduced. Smaller J values means conditions closer to the bollard pull condition, which again means that the propeller loading is increasing. Higher loading means that larger gradient have to be resolved, which again requires more of the numerical method. The results for small

J could probably have been improved by refining the mesh.

4. Bare hull simulation – with and without ice fins

The numerical appended hull model without propeller is calculated in a resistance test setup, where the model is positioned according to the measured dynamic sinkage and trim position and locked. The model speed is 1.915 m/s, which corresponds to a Froude number equal to 0.289 and a model Reynolds number equal to $Re=7.24$ million.

As mentioned above a grid stud was made for the hull model. Grid refinement between grids was obtained by applying a refinement factor of $\sqrt{2}$ to the mesh reference length when generating the three grids. The grid study shows that the calculated resistance changes 11.4% when going from coarse to medium grid, while the change is reduced 0.6% when going from medium to fine grid. A comparison between the computed fine-grid resistance and experimental data from the towing tank, [4], shows that the calculated resistance is under predicted with 2.4%.

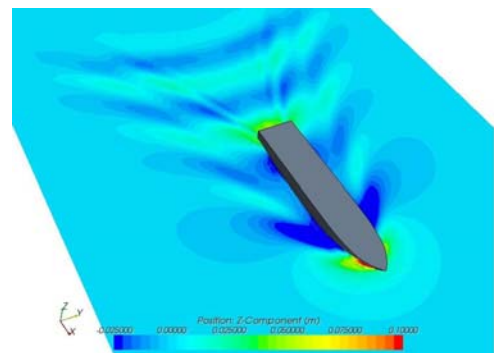


Figure 10: Calculated free surface elevation.

With respect to the field quantities the results are briefly summarized as follows: 1) High pressure occurs in the bow region where the flow is slowed down and the bow wave is formed due to stagnation. 2) The pressure decreases around the shoulders, where the flow is accelerated to get around and below the hull. 3) Further

downstream the pressure recovers and basically constant flow properties along the prismatic section of the hull are seen. 4) At the aft shoulders, i.e. the region where the hull form start to narrow in towards the stern and the water starts to flow into the wake region, the pressure decreases again. 5) The pressure increases again in the stern region and formation of the wake field with lower velocities is seen. The pressure field is not shown here. Figure 10 shows the calculated wave elevations around the ship and reveals a typical Kelvin wave pattern. Finally, Figure 11 shows the calculated nominal wake field behind the ship at a cross section located at the propeller plane. Due to the relatively slender shape of the ship, the bilge vortices, which normally are observed in the centre plane wake, are relatively weak. Consequently the contours appear smoother, and the traditional hook shape is not observed.

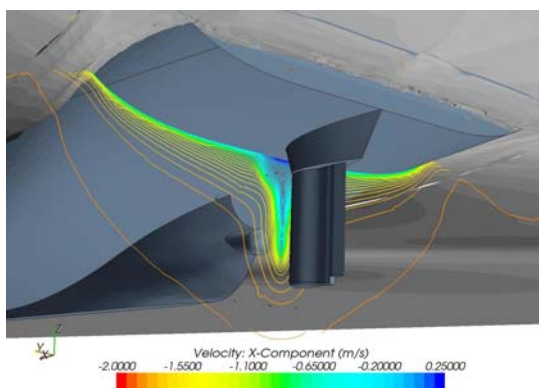


Figure 11. *Calculated wake field.*

The calculation above was conducted without ice fins, so in order to study the influence of the fins one additional computation was run with the ice fins included. The running condition was the same as above, i.e. model speed equal to 1.915 m/s, which corresponds to a Froude number equal to 0.289 and a model Reynolds number equal to $Re=7.24$ million.

5. Appended hull simulation – Cavitation tunnel setup

The goal of the present project is to simulate the complete ship with hull, rudder and propeller including the free surface around the ship. However, for the initial with-propeller calculations the problem was simplified by neglecting the free surface and using a setup similar to what is used in a cavitation tunnel. This means that only the underwater part of the ship was considered and a symmetry condition was applied on the still water surface. The model speed was 4.53 m/s, which corresponds to a model Reynolds number equal to $Re=17.1$ million. Atmospheric pressure was used in the simulation in order not to introduce cavitation on the propeller. Compared to the open-water calculation, which could be run in steady state mode, the simulation with the propeller behind the ship must be run in transient mode, i.e. time accurate. However, the different time scales of the propeller and the hull flow then become an issue in startup phase of the computation. The problem is that the time step is closely related to the rate of rotation of the propeller. In the present simulations the time step is chosen so the propeller rotates approximately three degrees per time step. This corresponds to time steps in the order of 3 to 5 10^{-4} sec. If the ship has to travel a couple of ships lengths in order for the boundary to build up on the hull this would take maybe 10 sec, so with the small time step this would take a very long time to calculate. In order to speed up the calculation the model was first run in steady mode with moving reference frame for the propeller. After the hull boundary layer then had developed, the transient solution was initiated and the propeller was rotated by means of a rigid body motion and sliding interfaces.

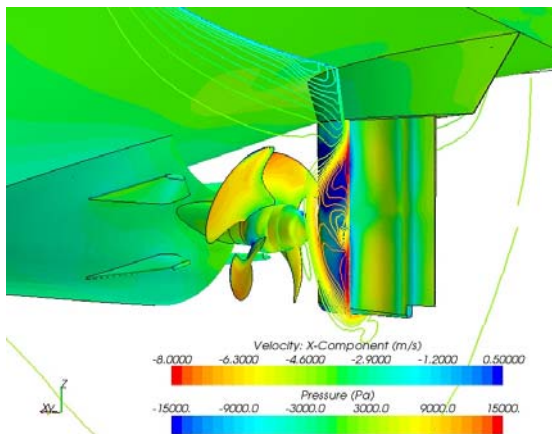


Figure 12. Calculated pressure on pressure side of propeller. Line contours represent the axial wake velocity.

A study of the field quantities, i.e. velocities and pressure in the stern region shows a time varying, but periodic flow field, which to a high degree is related to the blade frequency of the rotating propeller. Figure 12 and Figure 13 give an example of the pressure field in the stern region and the axial velocity contours in a cross section at the rudder position. With respect to the velocity field, it shows that the propeller accelerates the flow and introduces swirl in the flow downstream of the propeller. Consequently, the rudder sees an accelerated rotating flow field, which results in varying angles of attack along the span of the rudder. The pressure field on the propeller blades themselves varies with the blade position due to the non-uniform inflow field in the wake field. When the blade passes the centre plane wake around the twelve or six o'clock positions the low axial inflow velocity to the blade in these regions results in higher loading on the blade compared to when the blade is in the three o'clock position for instance. Also the loading depends on whether the blades move upwards in the wake (starboard side) or downward (port side). The reason is that the cross flow, which has an upwards direction on both sides results in different angles of attack for the blades which consequently experience different loadings.

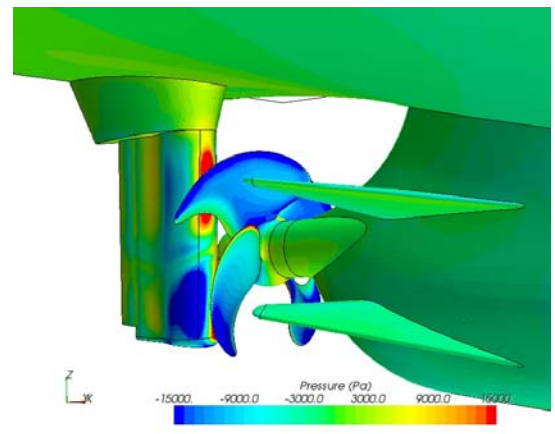


Figure 13. Calculated pressure on the suction side of the propeller.

The highest loading occurs on port side where the cross-flow and propeller motion have opposite directions. As seen the wake deficit of the hull strongly influences the propeller, but the propeller also influences the hull flow. The influence is most clearly seen in the pressure field. Upstream of the propeller the hull experiences suction, which reduces the pressure and increases the resistance. The effect is usually expressed as the thrust deduction. Another region of the hull that feels the presence of the propeller is the region above the propeller. In this region the passing blades will introduce pressure pulses on the hull, which in critical cases can lead to noise or vibration problems in the structure.

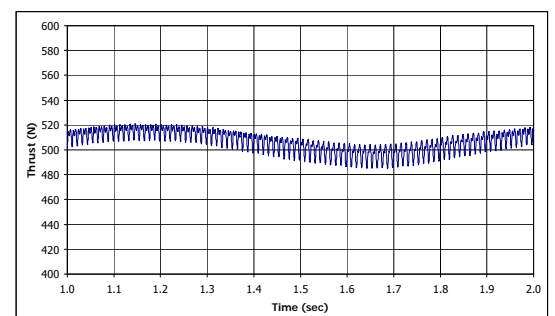


Figure 14. Time series for the calculated thrust.

Concerning the integral quantities for the present hull-propeller configuration, focus was placed on the propeller thrust and torque, since measured data for comparison was available from a

previous cavitation test [5]. Four different propeller loading conditions were calculated, but detailed results will only be discussed for one condition here. In this condition, the propeller was rotating with 22.57 rps. The time history of the calculated thrust and torque are shown in Figure 14 and Figure 15, respectively.

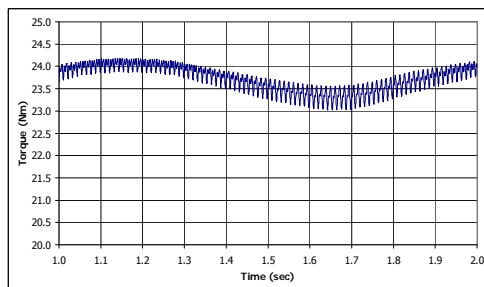


Figure 15. Time series for the calculated torque.

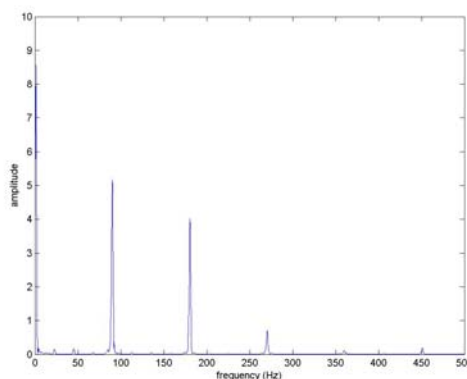


Figure 16: Frequency spectrum from FFT analysis of thrust signal.

From the two figures it is seen that the time series consist of a slowly varying signal overlaid with high frequency oscillations. In order to determine the dominant frequencies in the signals FFT analysis was used. Figure 16 shows the frequency spectrum for the thrust. Having a blade frequency of 90.3Hz it is seen that the dominant frequencies are multiples of the blade frequency. However, in addition to these frequencies there is also a peak at a very low frequency around 1Hz, but this should also be the case since Figure 14 and Figure 15 showed a slowly global variation in the signals. It is difficult to say exactly what causes this low

frequency behavior, but it is believed to come from the hull wake, which easily can be a little unsteady behind the ship. After studying the detailed behavior of the time series for the propeller quantities the mean values from the four calculations were compared with measured data from the cavitation tunnel.

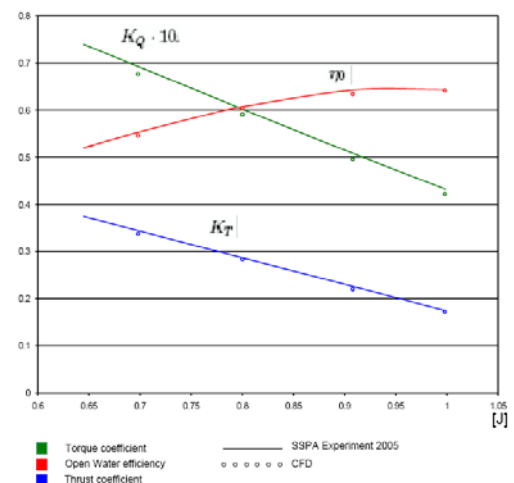


Figure 17. Comparison of measured and calculated propeller quantities.

Figure 17 shows the calculated propeller thrust, torque and efficiency together with the measured values.

Run No.	K_t	$K_q \times 10$	η_0
1	1.24	2.23	0.24
2	2.37	2.35	1.18
3	1.08	1.88	0.50
4	2.29	2.40	1.18

Table 3. Deviations between calculation and measurement for propeller behind ship condition in %.

Table 3 shows the deviations in %. It is seen that CFD slightly under predicts the quantities, but also the fairly good agreement is achieved. For the considered J values, the deviations seem to be slightly smaller compared to the open water calculation. It is difficult to say why this is the case, because the inflow field is somewhat more complicated than the uniform open-water inflow. One reason could be that the propeller mesh used behind the ship

is slightly finer than the open-water mesh and another could be that the computed wake field is a little different from the real inflow field which may cancel out some of the propeller errors. However, without measured velocity data for comparison this is not possible to say for sure.

6. Appended hull simulation – Towing tank setup

Until this point a number of simplified simulations have been conducted with the numerical model. The results for the resistance of the hull alone and the open water propeller quantities looks promising when compared to the model test results. This is also the case when the influence of the hull on the propeller is studied in the cavitation tunnel setup, where thrust and torque are predicted fairly well. However, one more thing has to be checked and that is the influence of the propeller on the hull, i.e. how well the resistance of the hull is predicted when the propeller is located behind the ship. The suction of the propeller on the ship. The suction of the propeller on the hull will be reflected as an increase of the resistance as is observed when doing self-propulsion tests in the towing tank. Therefore, the last calculation covers a simulation of the self propulsion test. In the present simulation, there is no searching for the self-propulsion point, so the applied propeller settings will be taken from the previous model test conducted in the towing tank.

The case considered is for a ship speed of 16 knots, which corresponds to a Froude number of 0.34. The applied model speed and propeller revolutions can be seen in Table 4.

Full scale speed	Froude numbre	Model scale speed	Model propeller revolution
16Kn	0.34	2.197 m/S	644 RPM

Table 4. Self-propulsion condition.

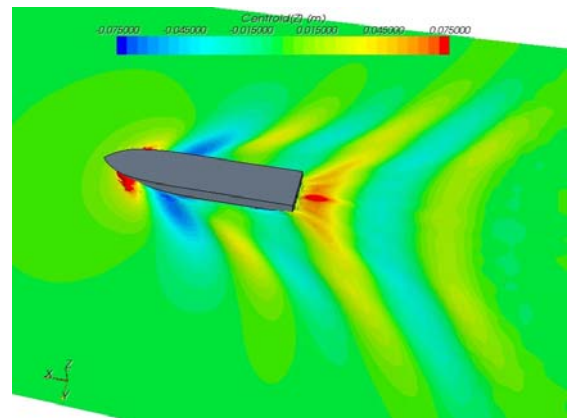


Figure 18. Global wave pattern.

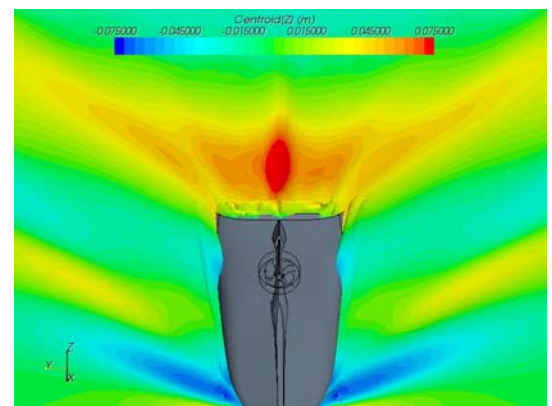


Figure 19. Local wave pattern in stern region.

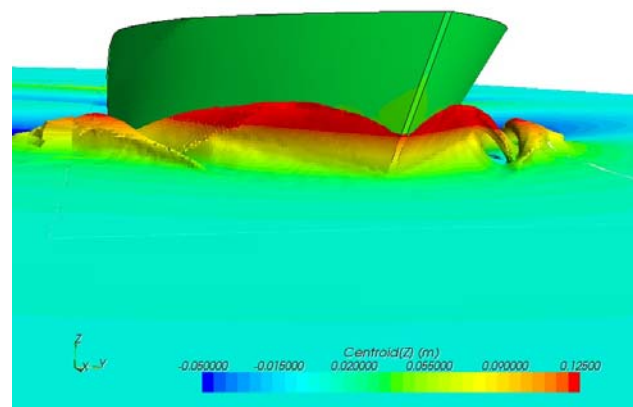


Figure 20. Local wave pattern in bow region.

Concerning the calculated results, Figure 18 shows the wave pattern around the ship and again a Kelvin type pattern is found. Locally, a few things can be observed. According to Figure 19 a typical stern wave pattern is observed, but it should be noted, that the wave

does not show centre plane symmetry. This is due to the presence of the propeller, which introduces rotation in the flow, which deforms the free surface behind the ship. Focusing on the bow, Figure 20 shows that the simulation captures the braking bow wave.

Figure 21 shows a photo of the wave profile along the hull during the model test and if the profile is compared qualitatively with the calculated profile in Figure 22 reasonable agreement is observed. Though, in the bow the calculated braking bow wave is relatively smooth and the spray that is observed in model test is not resolved in the present method. However, from a resistance point of view, the spray is a secondary effect and it is not assumed to influence the resistance significantly.



Figure 21. Wave profile on hull surface from model testing. Speed is 16kn.

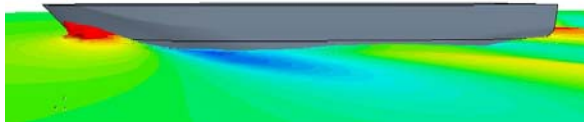


Figure 22. Wave profile on hull surface from CFD model. Speed is 16kn.

Concerning the flow field in the region around the stern, propeller and rudder the velocities and pressure show a time varying flow field. As for the computation of the cavitation tunnel setup at atmospheric pressure, the flow field shows some periodicity due to the blade frequency of the rotating propeller, but the unsteady behavior of the free surface disturbs the picture slightly. Figure 23 to Figure 26 give an example of the pressure field in the stern region. The pressure field on the propeller blades shows mainly negative pressures on the suction side of the propeller and mainly positive pressure on the pressure side, as expected. On the individual blades the pressure varies

with the blade position due to the non-uniform propeller inflow field in the wake field as discussed above in connection with the characteristics of the propeller flow in the cavitation tunnel setup. On the hull, the propeller introduces suction on the rear part of the hull upstream of the propeller. But in addition to this, the pressure field on the hull above the propeller also reflects the passing blades, which in the present figures increases the pressure in the considered region. It should be noted, that pressure distributions shown in Figure 23 to Figure 26 include the hydrostatic pressure, so that is the reason why the pressure generally seems to increase towards the bottom of the ship.

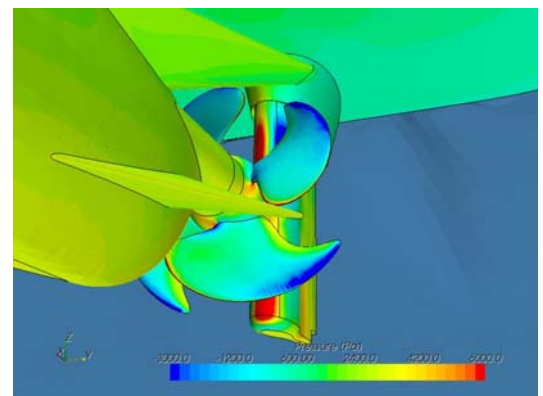


Figure 23. Pressure distribution on suction side of propeller. Port side.

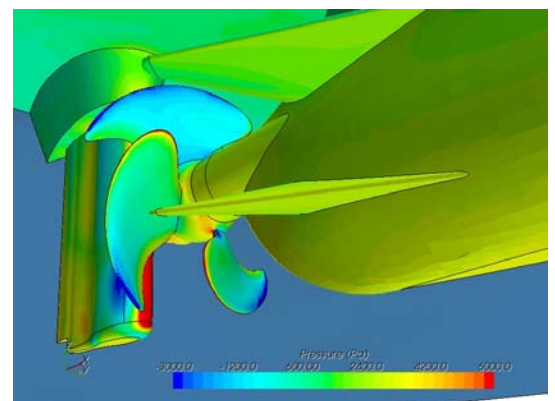


Figure 24. Pressure distribution on suction side of propeller. Starboard side.

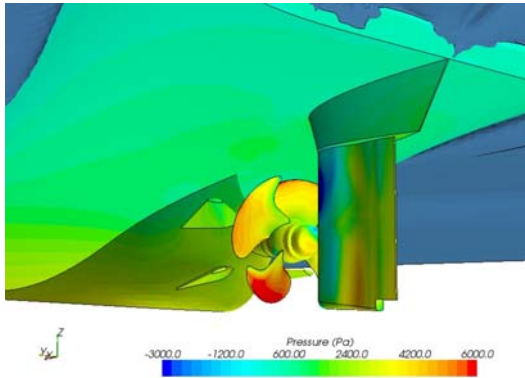


Figure 25. Pressure distribution on pressure side of propeller. Port side.

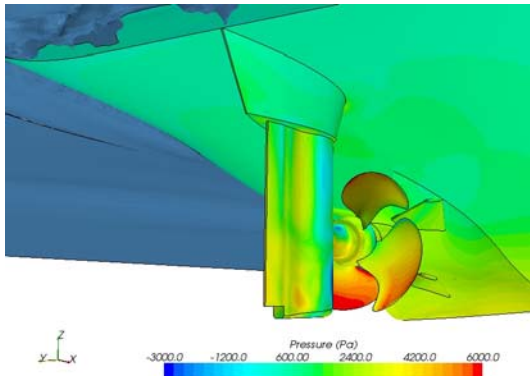


Figure 26. Pressure distribution on pressure side of propeller. Starboard side.

With respect to the streamlines on the hull surface, Figure 27 to Figure 30 show the streamline pattern on the hull and the skeg in the region around the ice fins. At the rear part of the skeg and in the region where the skeg and hull meet, a small zone with re-circulating flow is observed. However, this feature is quite common to see for this type of hull-skeg configuration. It should be noted, that the streamline plots are shown for a given instant of time. With the unsteadiness introduced by the rotating propeller, the streamline patterns will change depending on the position of the propeller.

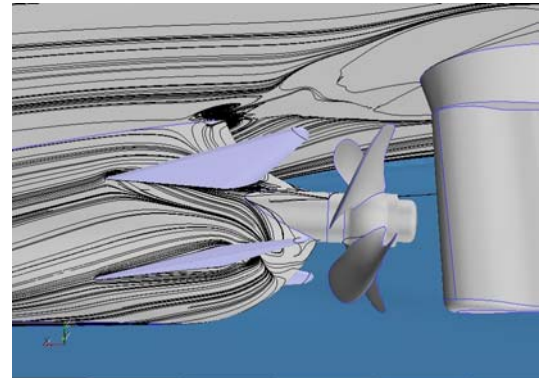


Figure 27. Streamline pattern on port side of hull. Top view of lower ice fin.

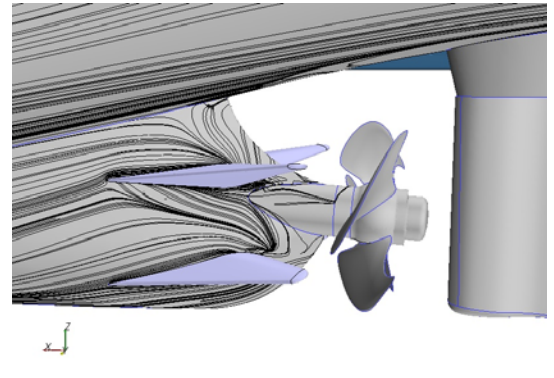


Figure 28. Streamline pattern on port side of hull. Top view of upper ice fin.

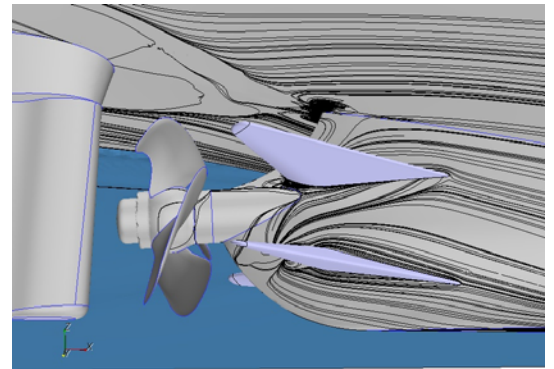


Figure 29. Streamline pattern on starboard side of hull. Top view of lower ice fin.

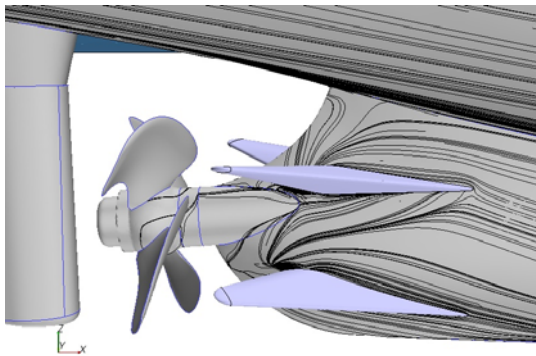


Figure 30. Streamline pattern on starboard side of hull. Top view of upper ice fin.

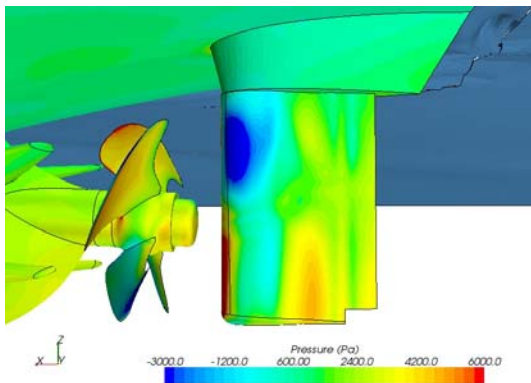


Figure 31. Pressure distribution on rudder. Port side.

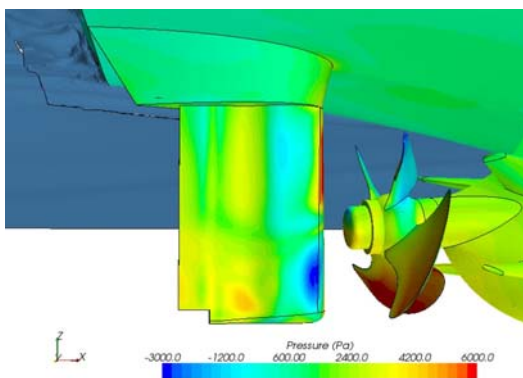


Figure 32. Pressure distribution on rudder. Starboard side.

When it comes to the rudder flow and the influence of the propeller on the rudder, two important effects can be found. One is that the propeller generally accelerates the axial flow over the rudder, which means that the

rudder will work more efficiently when deflected. The other is the change in local angle of attack along the rudder span and consequently also the pressure distribution. This effect is typically reflected in the fact that the neutral position of the rudder (zero lift) is not in the geometrical zero rudder angle position, but at an angle different from zero. Figure 31 and Figure 32 show the pressure distribution on port and starboard sides. The significant high and low pressure regions close to the leading edge are caused by the rotating propeller slip stream flow, which, as mentioned above, changes the local angle of attack. High pressure occurs where the slipstream hits the rudder and low pressure occurs on the opposite side which. Due to the rotational direction of the propeller the behaviour is opposite in the top and bottom of the slip stream.

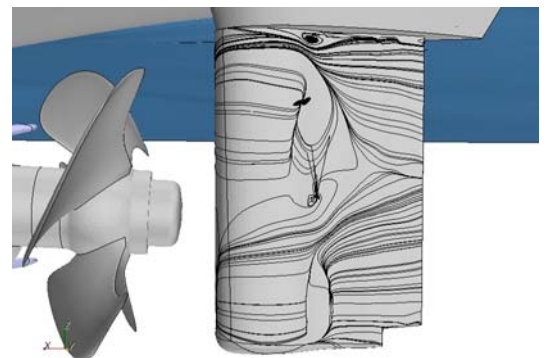


Figure 33. Streamline pattern on the rudder surface. Port side.

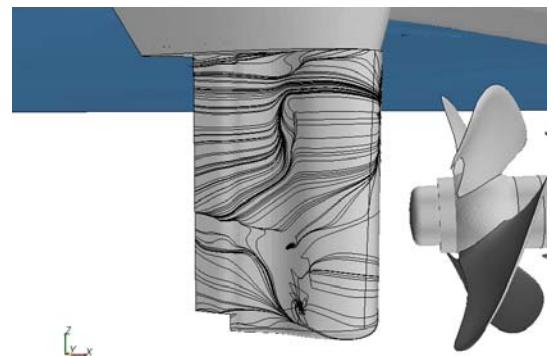


Figure 34. Streamline pattern on the rudder surface. Starboard side.

Figure 33 and Figure 34 show an instantaneous picture of the streamline patterns on port and starboard sides of the rudder. It is typical to see that the lines fan out on the part of the rudder where the rotating slipstream flow hits the rudder, i.e. lower part on port side and upper part of starboard side.

The last field quantities to be discussed are the velocities behind the propeller. Figure 35 shows the axial velocity distribution in a cross plane at the aft perpendicular. From the figure it is clearly seen how the propeller accelerates the flow in the slipstream. The maximum speed in the slipstream is close to two times the ship speed. Another thing to be noted is the concentrated low-velocity island at mid-span position on starboard side of the rudder. This feature is the centre of the hub vortex which is generated by the propeller. The low speed is due to the shadow of the hub. The vortex can also be seen in Figure 36 which shows the cross flow vectors. The same figure also shows the presence of the blade tip vortices. The vortices are strongest on port side of the rudder, where they are also most clearly seen. Another way to illustrate the vortices is to calculate the axial vorticity as shown in Figure 37. This type of plot will provide information about the strength and rotational direction.

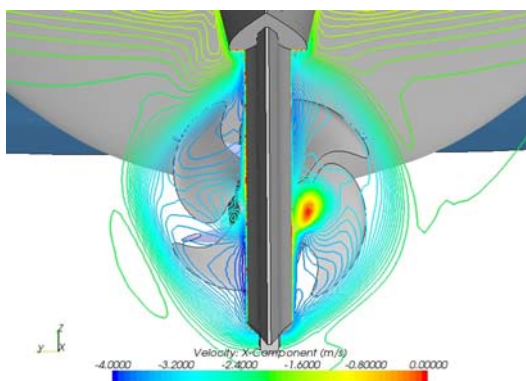


Figure 35. Axial velocity contours behind propeller in cross plane at AP.

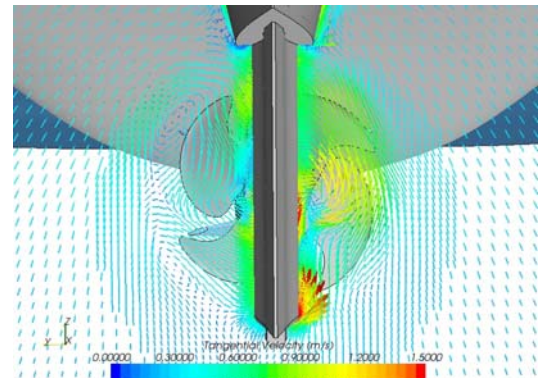


Figure 36. Cross flow vectors behind propeller in cross plane at AP.

Tracing vortex structures three dimensionally is sometimes useful in order to see for instance where the propeller blade tip vortices hit the rudder. For this purpose the so called Q-criterion is helpful. The criterion is based on iso-surfaces isolating areas where the strength of rotation overcomes the strain, which again means that these iso-surfaces give a picture of vortex envelopes. When using the Q-criterion, arbitrary positive Q-values can be used to make the iso-surfaces. However, there is no guideline for which value to use for vortex visualization, since this depends of the considered type of flow. If a value close to 0 is used, it becomes difficult to see the distinct vortex structures, so one has to find a level that will show the vortices. In the present case, $Q=500$ appears to work in order to see the propeller vortices. Figure 38 to Figure 40 show the blade tip vortices and the hub vortex.

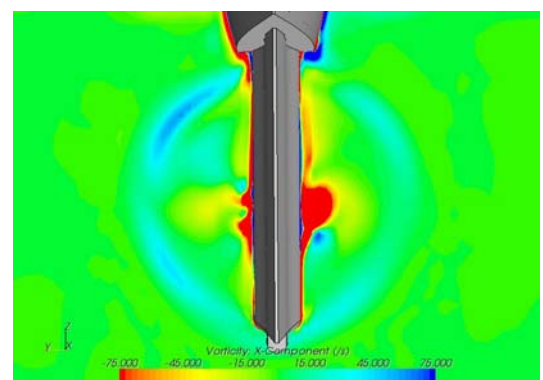


Figure 37. Axial vorticity contours behind propeller in cross plane at AP and 3D vortex visualization.

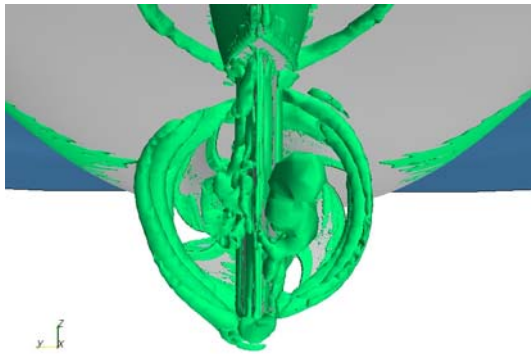


Figure 38. $Q=500$ iso surface. Seen from behind.

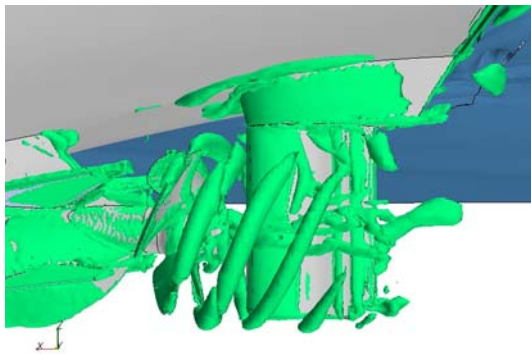


Figure 39. Vortex structures behind propeller. $Q=500$ iso surface. Port side.

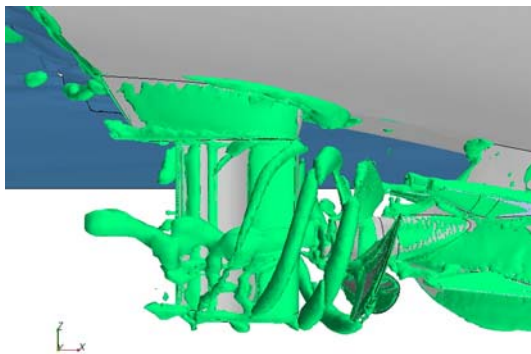


Figure 40. Vortex structures behind propeller. $Q=500$ iso surface. Starboard side.

One of the goals for simulating the present condition was to check how well the calculated hull and propeller quantities compare with measured data for the same condition. Table 5 shows propeller thrust and torque plus the

model resistance and the applied relaxation force, which usually is applied in connection with self propulsion tests. A comparison of the measured and calculated quantities shows that CFD slightly over predicts the quantities, but on an overall level fairly good agreement is achieved, which is encouraging from the point of view of practical application in connection with ship design process.

	EXP	CFD	Diff . %
Fr.	0.34	0.34	-
Prop (rpm)	644	644	-
K_t	3.57E-1	3.66E-1	2.5
K_q	7.158E-2	7.158E-2	0.1
C_{tmodel}	9.89E-3	1.02E-2	3.1
C_{relax}	7.47E-4	8.21E-2	9.9

Table 5. Comparison between measured and integral quantities.

7. Cavitation setup

To make an initial test of STAR-CCM+ 's capability to capture cavitation, on the propeller blades and in the tip vortices downstream of the propeller, the cavitation model, which is based on the Rayleigh-Plasset model, was turned for a condition similar to one of the experimental cavitation tests.

In order to simulate the cavitating propeller a refined mesh consisting of approximately 13 million cells was made. The additional cells were primarily concentrated around the propeller tips and in the region where the tip vortices were expected to be located. Since cavitation is a transient phenomenon, the simulation was run in transient mode. Further, the rotating propeller was modelled by means of Rigid Body Motions and sliding interfaces between propeller and hull domain.

Figure 41 and Figure 42 shows the propeller cavitation as observed in the cavitation tunnel. A comparison with the computed results in Figure 43 shows that the experiment and the calculation qualitatively agree when it comes to the

extend of the cavitation bubble on the propeller blade in the tip region.



Figure 41. *Visualization of tip vortices during cavitation test.*

However, when it comes to the cavitation bubble in the tip vortices in the slipstream behind the propeller, the computation seem to be too dissipative to maintain the tip vortex cavitation. As shown earlier for instance in Figure 39, the tip vortex can be traced over the rudder, but it appears that the pressure in the core of the tip vortices is not low enough to maintain the vapour bubble.



Figure 42. *Vizualization of the tip cavitation on the propeller blades.*

As mentioned in the beginning of this section, the cavitation modelling was only intended to be an initial test of the capabilities. It is not within the scope of this project, to conduct a detailed study of the cavitation. Therefore, no effort has been made to improve the results

above by studying issues related to for instance discretization scheme, turbulence modelling or mesh density. This should be done in future work.

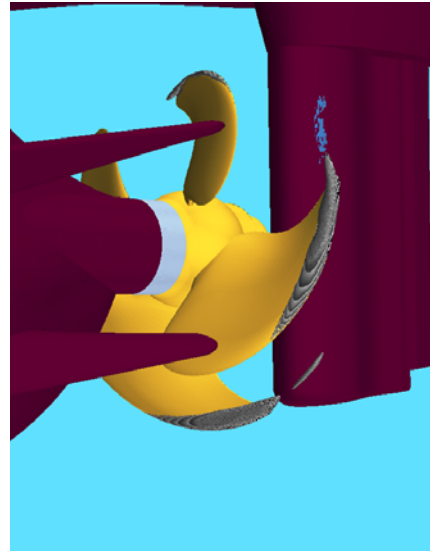


Figure 43. *Computed extension of cavitation on blades and in tip vortices.*

8. Summary and conclusions

In the present work RANS simulations have been conducted for: a propeller in open water, an appended ship in a resistance test setup, a combined ship-propeller configuration in a cavitation tunnel setup at non-cavitating and cavitating conditions and an appended self-propelled ship in a resistance test setup. The open water and resistance calculations were steady state computations, while the combined hull-propeller cases were run time accurate. Grid studies were made for the open water propeller and the appended hull calculation. A formal verification was not conducted, so the grid uncertainty was not estimated. Only changes in solutions between grids were considered. For the medium and fine grid solutions the two studies showed changes in integral quantities between grids of 1.6% and 0.6%, respectively. Concerning the results of the calculation all five considered configurations showed promising results:

The open-water calculation showed that thrust and torque could be predicted within 3.5% and 0.5% of measured data, respectively, at the point where the propeller works when behind the ship. At higher propeller loadings, i.e. lower J , larger deviations were observed. A couple of reasons for this behavior could be that the grid was not fine enough to resolve this condition and/or the turbulence model has limitations when the propeller loading increases.

For the resistance test setup, the simulation showed a typical ship flow field and the resistance was predicted within 2.4% of measured data.

The simulation of the cavitation tunnel setup at atmospheric pressure, showed a complex time varying flow field and mutual interaction between hull, rudder and propeller. When compared to measured data it was found that CFD predicted both thrust and torque within 2.4% of the measured data. When the pressure was lowered in order to allow cavitation, the results showed that the cavitation on the propeller blades qualitatively was captured in the tip regions of the blades, when compared to experiments. However, the bubbles in the tip vortices downstream of the propeller were not captured. The cavitation modeling requires more work

to be studied in more detail, but that was not a part of the present project.

Finally, for self-propelled ship, the integral quantities were also in reasonable agreement with the measured data. The resistance was predicted within 3.1% of measured data, while the thrust and torque were within 2.5%. Concerning the overall flow field, the only comparison between CFD and EFD was done qualitatively for the near-hull free surface elevation. It was found that the calculated and measured surface elevations agreed fairly well.

9. Literature

- [1] Simonsen, C.D. and Stern, F., "RANS maneuvering simulation of Esso Osaka with rudder and a body-force propeller," *J. of Ship Research*, Vol 49, No. 2, June 2005.
- [2] Carstens, R., Numerical investigation of flow around a ship's hull and cavitation prediction using RANS CFD, Master thesis, Aalborg University, Denmark, 2008.
- [3] StarCCM+ Users manual
- [4] FORCE Technology report no. 2005072-4B (Confidential)
- [5] SSPA Report no. 20053790-1 rev A. (Confidential)